BNL-225765-2024-JAAM

Solvent-Mediated, Reversible Ternary Graphite Intercalation Compounds for Extreme-Condition Li-Ion Batteries

L. Tao, S. Hwang

To be published in "Journal of the American Chemical Society"

March 2024

Center for Functional Nanomaterials

Brookhaven National Laboratory

U.S. Department of Energy

USDOE Office of Science (SC), Basic Energy Sciences (BES). Scientific User Facilities (SUF)

DISCLAIMER

Solvent-mediated, reversible ternary graphite intercalation compounds for extreme-condition Li-ion batteries

Lei Tao[1*&], Dawei Xia[1&], Poom Sittisomwong[2], Hanrui Zhang[3], Jianwei Lai[3], Sooyeon Hwang[4], Tianyi Li[5], Bingyuan Ma[2], Anyang Hu[1], Jungki Min[1], Dong Hou[1], Sameep Rajubhai Shah[6], Kejie Zhao[6], Guang Yang[7], Hua Zhou[5], Luxi Li[5], Peng Bai[2], Feifei Shi[3], Feng Lin[1,8*]

[1] Department of Chemistry, Virginia Tech, Blacksburg, VA 24061, USA

[2] Department of Energy, Environment & Chemical Engineering, Washington University in St. Louis, St. Louis, MO 63130, USA

[3] Department of Energy and Mineral Engineering, The Pennsylvania State University, University Park, PA 16802, USA

[4] Center for Functional Nanomaterials, Brookhaven National Laboratory, Upton, NY 11973, USA

[5] X-Ray Science Division, Argonne National Laboratory, Lemont, IL 60439, USA

[6]Mechanical Engineering, Purdue University, West Lafayette, IN 47907, USA

[7] Chemical Sciences Division, Oak Ridge National Laboratory, Oak Ridge TN 37830, USA

[8] Department of Materials Science and Engineering, Virginia Tech, Blacksburg, VA 24061, USA

[*]Corresponding Authors: taolei@vt.edu; fenglin@vt.edu.

Abstract: Traditional Li-ion intercalation chemistry into graphite anode exclusively utilizes the co-intercalation-free or co-intercalation mechanism. The latter mechanism is based on ternary graphite intercalation compounds (t-GICs), where glyme solvents were explored and proved to deliver unsatisfied cyclability in LIBs. Herein, we report a novel intercalation mechanism, that is, *in-situ* synthesis of t-THF-GICs in the tetrahydrofuran (THF) electrolyte via a spontaneous, controllable reaction between binary-GICs and free THF molecules during initial graphite lithiation. The spontaneous transformation from b-GIC to t-GIC, which is different from conventional co-intercalation chemistry, is characterized and quantified via *operando* synchrotron X-ray and electrochemical analyses. The resulting t-GIC chemistry obviates the necessity for complete Li-ion desolvation, facilitating rapid kinetics and synchronous charge/discharge of graphite particles even under high current densities. Consequently, the graphite anode demonstrates unprecedented fast charging (1 min), dendrite-free low-temperature performance, and ultralong lifetimes exceeding 10,000 cycles. Full cells coupled with layered cathode, display remarkable cycling stability upon a 15-min charging and excellent rate capability even at -40 °C. Furthermore, our chemical strategies are shown to extend beyond Li-ion batteries to encompass Na-ion and K-ion batteries, underscoring their broad applicability. Our work contributes to the advancement of graphite intercalation chemistry and presents a low-cost, adaptable approach to achieving fast-charging and low-temperature batteries.

Keywords: Li-ion batteries, ternary graphite intercalation compounds, co-intercalation, fast charging, low temperature

Introduction

Graphite intercalation compounds (GICs) have shown programmable physiochemical properties for applications such as electrical conductors, catalysis, hydrogen storage, and energy storage[1–3]. Among these, alkali-ion based GICs are particularly attractive as electrodes for rechargeable batteries[1,4]. GICs exhibit tunable guest-host interactions with anions, cations, and solvated cations, enabling different battery chemistries[5,6]. One of the most extensively studied GICs is lithiated graphite (LiC_6), a binary GIC (b-GIC) serving as the anode in commercial Li-ion batteries (LIBs)[7]. Researchers synthesized LiC_6 from graphite via chemical means in the 1950s[8], but it took over three decades to synthesize it electrochemically[9–11]. The electrochemical synthesis is more intricate, governed by the solvation structure, the thermodynamic properties of electrolytes, and the graphite-electrolyte electrochemical interphase[12]. In conventional graphite intercalation chemistry, the interphase allows cations to transport while blocking other electrolyte components such as solvent molecules[13]. Ternary-GICs (t-GICs) is another category of GICs, which have cations and solvent molecules co-intercalated and offer excellent chemical and structural tunability[14]. Typically, a single reaction can only lead to either b-GIC or t-GIC, and the co-existence of and interconversion between b-GIC and t-GIC have not been reported in battery chemistry.

Bidentate ligands such as dimethoxyethane (DME) have strong chelating effects with Li ions, resulting in facile Li-solvent co-intercalation upon electrochemical cycling and chemical pre-lithiation of graphite[15,16]. Unidentate cyclic ether ligands such as tetrahydrofuran (THF) have unique electrochemical and chemical interactions with graphite, which can potentially enable dynamic interconversion between b-GICs and t-GICs even under battery operating conditions. When solvating Li ions, THF has a higher coordination number than bidentate ligands[17], suggesting lower desolvation energy and less tendency to be co-intercalated with cations during electrochemical reactions. However, the earlier literature reported the ternarisation of stage 1 KC_{24} in THF solvent leading to the formation of a stage 2 $K(THF)_2C_{20\sim30}$ t-GIC (i.e., chemical reaction)[18]. Therefore, such a discrepancy between electrochemical and chemical reactions implies that hybrid intercalation and co-intercalation reactions are possible, which can then offer a dynamic interconversion between b-GICs and t-GICs.

The dynamic interconversion between b-GICs and t-GICs is far beyond advancing the fundamental insights into intercalant-graphite interactions and shows great practical promise for designing

extreme-condition batteries[19]. t-GICs have outstanding electrical conductivity and fast diffusion of solvated ions between graphene layers[14]. Furthermore, the energy barrier of the charge transfer process is lowered due to the co-intercalation mechanism[6,20,21]. In fact, a plethora of Li-t-GICs have been explored by using glyme solvents to make use of these advantages, but the cycling stability issues have remained unresolved, which can be due to the large volume expansion of lithiated graphite (>200%)[15]. Given the weaker interaction with Li-ion compared to glyme solvents, we hypothesize that unidentate ligand THF can be an alternative to ignite new co-intercalation chemistry for extreme-condition batteries, especially for fast-charge and low-temperature applications. Last but not least, THF brings tremendous cost reduction as an electrolyte solvent compared to commercial electrolyte solvents and other solvents under development.

Herein, we report a t-THF-GIC displaying an ultralong lifespan of over 10,000 cycles with high Coulombic efficiency (CE) and negligible capacity decay, one-minute fast charging (100% retention), and unprecedented low-temperature performance without Li plating. Such new co-intercalation chemistry with high stability has never been achieved in traditional glyme solvents. We discovered *in-situ* b-GICs to t-GICs transformation during the initial cycles, which can be modulated by current density, temperature, SEI properties, and graphite type. The *in-situ* chemical synthesis of t-THF-GIC can proceed through uptaking THF molecules from the electrolyte in the absence of a dense and continuous SEI. Paired with the NMC cathode, the full cell displays outstanding cycling stability with a 15-minute charging. Even at -40 °C, the excellent rate capability can be achieved. The graphite anode with such an innovative operation mechanism has led to the best performance co-intercalation based batteries reported thus far. Our study has enriched the knowledge library for graphite intercalation chemistry through a suite of *operando* characterization and represents a leap for Li-ion chemistry operating under extreme conditions.

Results and Discussion

Chemical reaction between b-GICs and THF hidden during the first cycle

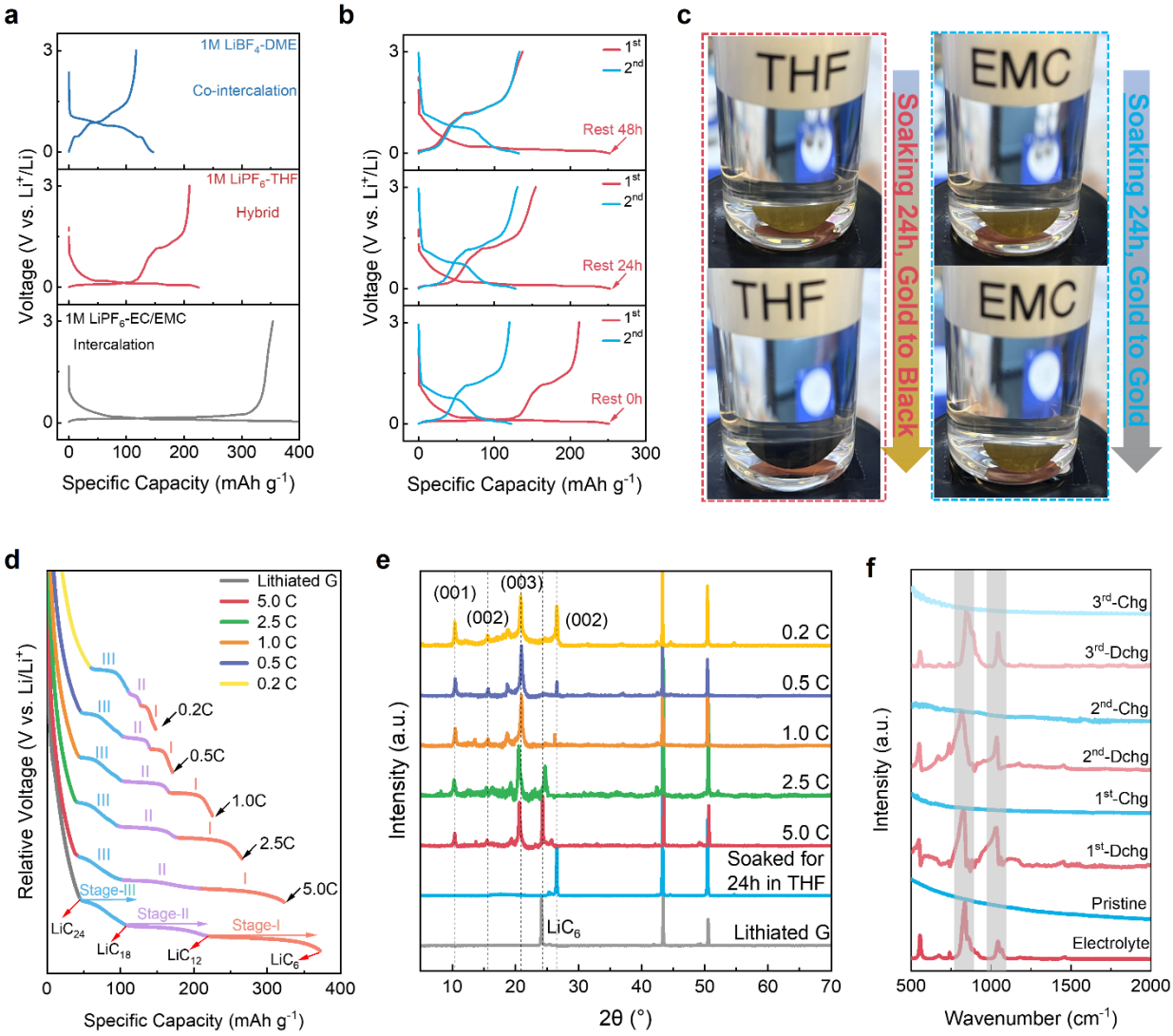

Fig. 1: Chemical reaction between b-GICs and THF hidden during the first cycle in THF-based electrolytes. a, Discharge-charge curves of the graphite anode cycled in 1M $LiPF_6$-EC/EMC (co-intercalation-free), 1M $LiPF_6$-THF (co-intercalation-free to co-intercalation), and 1M $LiBF_4$-DME (co-intercalation) at 1C (1C=100 mA g^{-1}). **b**, Discharge-charge curves of the graphite anode cycled in the 1M $LiPF_6$-THF electrolyte with different resting durations after the 1st lithiation (0, 24, and 48h). **c**, Photographs of fully lithiated graphite (LiC_6) before and after soaking in THF and EMC solvents. **d**, The 1st discharge curves of the graphite anode cycled in the 1M $LiPF_6$-THF electrolyte at a current range of 0.2 to 5 C. A graphite with a complete lithiation

process, showing typical three evolution stages (III, II, I), is provided as a comparison to observe the differences in the three stages under different currents. **e**, XRD patterns of the graphite anodes after the 1st discharge shown in **c** and **d**. **f**, FTIR spectroscopy of the graphite anodes cycled in the 1M $LiPF_6$-THF electrolyte and measured after different cycling histories (Notably, after the 1st discharge, the cell was rested for one day before being dissembled).

We use superior graphite as the platform, and Fig. S1 shows the morphology and structure details. Graphite anode has been perceived to reversibly store mobile ions in a single storage mechanism, that is either intercalation or co-intercalation. **Fig. 1a** demonstrates the intercalation in the EC/EMC-based electrolyte and the co-intercalation in the DME-based electrolyte. The voltage profiles and the corresponding *dQ/dV* curves show common intercalation or co-intercalation plateaus (Fig. 1a, Fig. S2a). When using 1M $LiPF_6$-THF electrolyte, we observe interesting phenomena: (1) the first lithiation shows a co-intercalation-free mode, while the first delithiation is a combination of co-intercalation and intercalation (Fig. 1a). The corresponding *dQ/dV* curves are asymmetrical (Fig. S2a). (2) The second lithiation is predominantly co-intercalation and is highly reversible (Fig. 1b). The co-intercalation-free feature can be explained by the weak Li^+-THF binding (discussed in MD simulation), especially compared to glyme counterparts. The co-intercalation contribution during the first delithiation can only arise from the chemical reaction between b-GIC and THF molecules in the electrolyte. The underlying b-GICs to t-GICs transformation will be discussed in a subsequent section. In this section, we majorly present electrochemical analyses to elucidate the *in-situ* formation of t-GICs in operating batteries. We first demonstrate the tailorable Li storage mechanism in the 1st cycle. As shown in Fig. 1b, the capacity contribution from deintercalating Li ions decreases if we rest the cell after the first lithiation. Especially after a 48h rest, the capacity contribution from deintercalating Li ions disappears, and the charging curve overlaps with the 2nd charge. These results show that the *in-situ* b-GICs to t-GICs transformation is not completed immediately following the formation of b-GIC.

Then, we investigate how *in-situ* transformation is governed by the reaction environment. We first study the pure chemical reaction without the influence of the electrical field by soaking lithiated graphite (i.e., LiC_6) in THF and EMC solvents. We observe a golden-to-black color change only in the THF solvent after 24h (Fig. 1c). In battery cells, the discharge capacity anomalously increases as the current density increases from 0.2 to 5 C (Fig. 1d, Fig. S2c). Specifically, the stage

II to stage I conversion of lithiated graphite is less pronounced when a low current density is used (Fig. 1d, Fig. S2b-c). When the cells are rested after the initial discharge, a decrease in the following charge capacity is consistently observed, especially for the cells cycled at high current densities (Fig. S2d). We conjecture that at low current densities or during the rest, there is ample time for THF to react with b-GICs. Once b-GICs transform into t-GICs, they cannot proceed to form b-GICs with a lower stage. Considering the diverse morphologies of graphite materials, we also investigated the b-GICs to t-GICs transformation using mesocarbon microbeads (MCMB) and natural graphite (NG), as shown in Fig. S3. We find that the cycle number needed for the transformation is different. MCMB requires more cycles to reach stable capacity (complete transition of b-GIC to t-GIC). Another finding is that the ultimate capacity is identical in different graphite materials (Fig. S3c). These data support our hypothesis that b-GIC reacts with free THF to form t-GIC.

The XRD patterns further show that the LiC_6 characteristic peaks weaken after soaking in THF or cycling at low current densities (Fig. 1e). We conclude that the b-GIC can have two phase transformation pathways: (1) further electrochemical lithiation to form lower-stage b-GIC, and (2) chemical reaction with free THF molecules in the electrolyte. At a low current density, the reactions are more concurrent, leading to more formation of t-GICs. Interestingly, the same chemical reaction also occurs in the G||Na system (Fig. S4) and even in the G||K system (Fig. S5), breaking the conventional wisdom that cyclic ether cannot reversibly co-intercalate into graphite[22,23].

The *in-situ* formation of t-GIC can be affected by the SEI composition and thickness, which is associated with the stability of salts and solvents. When we switch from $LiPF_6$ to LiFSI, more LiC_6 is formed during the first lithiation, but the b-GICs to t-GICs transformation is less pronounced (Fig. S6a-b). The co-intercalation behavior still occurs, but irreversibly, leading to rapid capacity decay of the G||Li cell (Fig. S6c). We observe thicker SEIs cycled in the 1M LiFSI-THF electrolyte, which hampers the interaction between b-GIC and free THF molecules (Fig. S7). The graphite anode cycled in 1M $LiPF_6$-THF exhibits clean surfaces without SEI formation or ultrathin SEI sporadically distributed, consistent with its high ICE (Fig. S2c, S8a-e). The clean graphite surface explains the high reversibility of the Li^+-THF co-intercalation. Such differences in SEI properties have led to drastically different kinetics. The desolvation energy and the energy for Li^+ transport

through SEI are shown in Fig. S9. The desolvation energies of the two electrolytes remain at almost the same value, i.e., 34 vs. 32 kJ mol^{-1} (Fig. S9c). This is also consistent with the voltage profile of the G||Li cell that incomplete desolvation leads to solvent co-intercalation into graphite. However, the activation energy for Li^+ transport through SEI in the $LiPF_6$-THF electrolyte is significantly lower than that in the LiFSI-THF electrolyte (Fig. S9d).

We then examine the structural changes of graphite due to the b-GICs to t-GICs transformation using *ex situ* FTIR and Raman spectroscopy. Compared with pristine graphite, the Li^+-THF characteristic FTIR peaks emerge after full discharge (including the first discharge), and then disappear after full charge (Fig.1f). This directly manifests the uptake of free THF molecules and the b-GICs to t-GICs transformation. Meanwhile, Li^+-THF co-intercalation is highly reversible. Fig. S10 shows the *ex situ* Raman spectroscopy of graphite during cycling. The pristine graphite exhibits a weak D band (1350 cm^{-1}) and a strong G band (1600 cm^{-1}), with an I_D/I_G ratio of 0.25. During the 1st discharge, the intensity of the D band increases significantly, implying that the well-ordered graphitic interlayers become disordered due to structural changes caused by the THF uptake. During the 1st charge, the intensity of the D and G bands cannot return to their original state. The same phenomenon is observed in the 2nd and 3rd cycles, while the I_D/I_G ratio increases from 0.25 to 0.28, suggesting an increase in structural disorder attributable to repeated Li^+-THF co-intercalation. *Operando* optical microscopy of graphite during cycling is shown in Video S1. Only a slight yellowish change occurs during the first discharge, indicating the presence of LiC_6, while in subsequent cycles, the graphite remains black with volume expansion, verifying the co-intercalation behavior (Video S1).

***Operando* characterization of the b-GIC to t-GIC transformation mechanism**

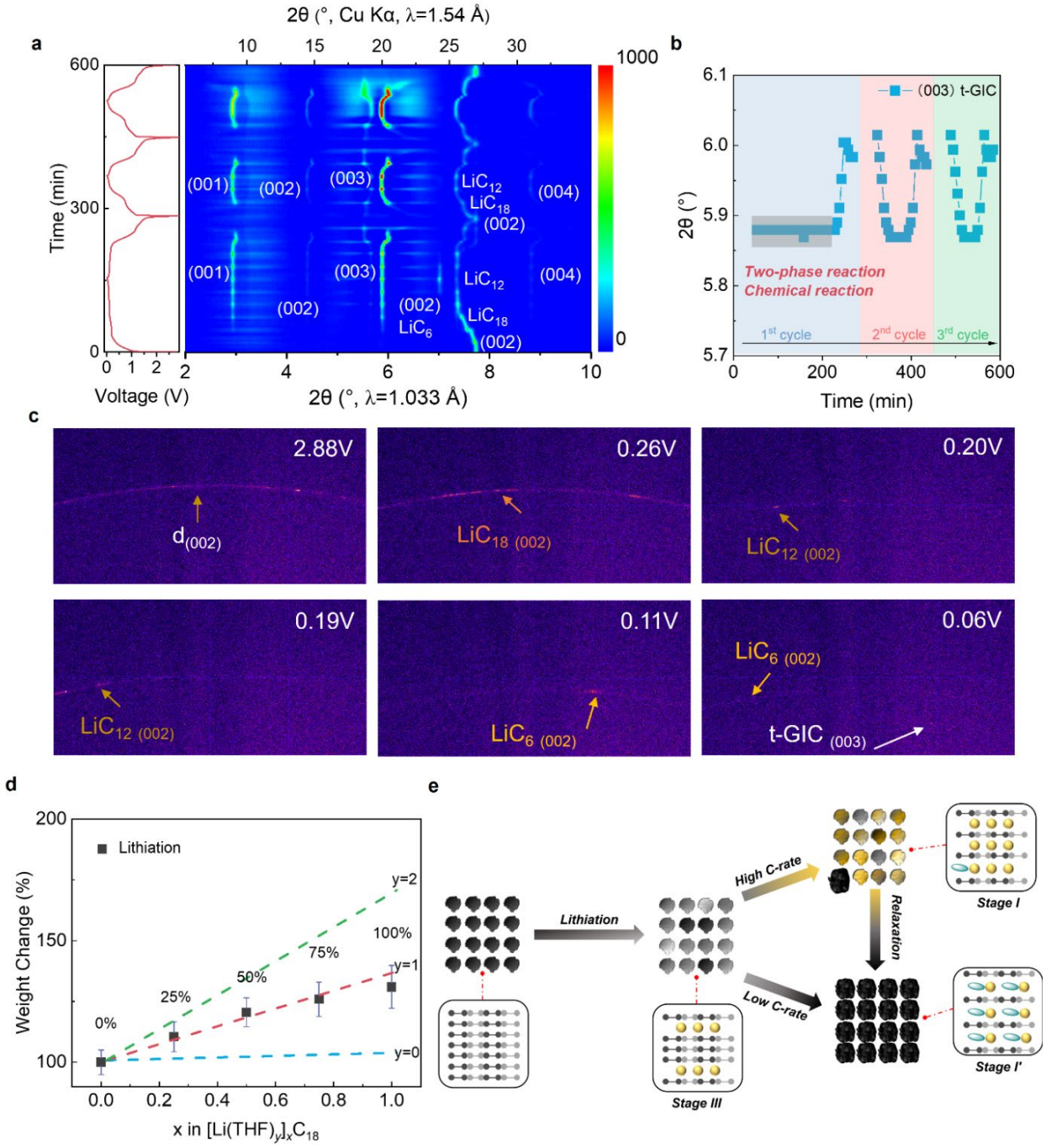

Fig.2: *Operando* characterization of the b-GIC to t-GIC transformation mechanism. a, *Operando* synchrotron XRD patterns and galvanostatic charge-discharge curves of the G||Li cell at 1C for 3 cycles. **b**, The evolution of t-GIC (003) peak during the first 3 cycles. **c**, CMCD to show the synchronous discharging (1st discharge) among different graphite particles. **d**,

Measurements of the weight changes of the graphite at different discharge states to estimate the number of co-intercalated THF. The error bars are created based on the standard deviation of three repeated measurements. **e**, Schematic illustration of the *in situ* t-GICs synthesis during the 1st lithiation.

The structural evolution of graphite is further investigated by *operando* synchrotron XRD (Fig. 2a, Fig. S11). The pristine graphite displays a strong (002) diffraction peak at 7.7°. During the 1st discharge, graphite undergoes lithiation to form b-GIC LiC_{18} and LiC_{12}, as evidenced by the shift of (002) peak towards low angles. At stage II (~0.12 V), Li^+-THF t-GIC gradually emerges as shown by three new peaks at lower angles and one new peak at higher angles, corresponding to the (001), (002), (003), and (004) planes of graphite, respectively. Since the lithiation voltage profile shows no co-intercalation feature between 0.4~0.7 V, the emergence of Li^+-THF t-GIC is caused by the chemical reaction between b-GIC and free THF molecules. Upon the subsequent charge, these new peaks shift back reversibly and disappear at the end of the charge. However, the (002) peak is weakened due to the increasing structural disorder. Such a reversible evolution of the (002) peak is observed in the subsequent cycles, but the LiC_6 peak no longer appears (Fig. S11), suggesting a pure Li^+-THF co-intercalation behavior with excellent reversibility. Fig. 2b delineates the position of the t-GIC (003) peak along with cycling time. The t-GIC (003) peak at 5.87° emerges at 52.7 min during discharging due to the b-GIC to t-GIC transformation. The asymmetric behavior of structural evolution in the first cycle agrees well with the asymmetric voltage profile and the proposed *in-situ* b-GICs to t-GICs transformation. After the 2nd and 3rd cycles, the peak shift is highly symmetric, consistent with excellent reversibility of Li^+-THF co-intercalation. The *ex-situ* XRD patterns further characterize the evolution of graphite diffraction peak after the 10th and 100th cycles, where the (002) peak of both shows similar intensities (Fig. S12). These results demonstrate that the Li^+-THF co-intercalation in the graphite is highly reversible, and the interlayer structure of graphite is highly stable during extended cycling.

This transformation mechanism completely differs from the traditional electrochemical pathway to form t-GICs (i.e., DME or diglyme co-intercalation)[15,24]. It is well known that DME has a strong chelating effect with Li-ion. As such, t-GIC directly forms during the first lithiation process (Figure 1a, Fig. S13)[24]. The lithiated graphite (LiC_6) soaking experiment also shows the difference between THF and DME in transforming b-GIC to t-GIC (Fig. S14). After one day of soaking, the

color of both LiC_6 electrodes turned black, confirming the chemical reaction between LiC_6 and free solvents. However, the electrode soaked in THF remained on the current collector even when shaken vigorously, while the electrode soaked in DME got peeled off and pulverized completely (Fig. S14). These results indicate that the reaction between THF and b-GIC is milder, and the volume expansion of t-THF-GIC is much smaller than that of t-DME-GIC. This is also consistent with the XRD result (Fig. S13). The XRD patterns of specific stages are extracted from the two *operando* XRD (Fig. S13b). We calculated the volume expansion of t-GICs formed from these two electrolytes (Fig. S13c). The t-THF-GIC has a smaller interlayer spacing Ic=0.88 nm and a much lower volume expansion (163%) compared to the t-DME-GIC counterpart. Fig. S13d compares the maximum intensity of (003), which indicates the fraction of t-GIC over b-GIC. In the THF-based electrolyte the value gradually increases with cycle number, while in the DME-based electrolyte, it directly reaches a high value because the Li^+-DME co-intercalation happens in the very first lithiation. These results show that the smaller volume expansion in t-THF-GIC and the gradual b-GIC to t-GIC transformation enable better mechanical properties for the electrode. Moreover, the Li^+-DME co-intercalation has a significantly lower diffusion coefficient in graphite than the Li^+-THF co-intercalation, resulting in a larger Li^+-DME concentration gradient in graphite and creating a much larger mismatch strain (more discussion shown in Fig. S15).

The *operando* coherent X-ray multicrystal diffraction (CMCD) technique can capture the structural transformation of graphite particles, with each diffraction spot representing a particle. We use CMCD to monitor if these particles have synchronous reactions (Fig.2c, Video S2). In Fig. 2c, the image captured at the open circuit voltage (OCV) shows a single ring composed of sequential bright diffraction spots, which correspond to c-axis reflections of tens of graphite particles. During the 1st discharge, the bright spots shift synchronously, then gradually weaken due to the formation of b-GICs (stage III). Further lithiation, some b-GICs (stage III) can transform to higher-stage b-GICs (stage I, LiC_6), whereas some b-GICs transform to t-GICs by chemically reacting with THF. Such a buffer transition path makes the volume expansion of graphite smaller, thus achieving a stabler fast-charging electrode, which also differs from the traditional DME co-intercalation (Fig. S16). In subsequent cycles, the weak ring moves reversibly, indicating that the co-intercalation is highly reversible (Video S2). We further determine the stoichiometry of t-GIC based on the following equation:

$$C_n + e^- + Li^+ + yTHF \rightleftharpoons Li^+(THF)_y C_n^-,$$

According to the voltage profile of the G||Li cell (Fig. 1b), the measured reversible capacity of graphite after fully discharging is ~120 mAh g^{-1}, indicating that one $Li^+(THF)_y$ complex contains 18 carbon atoms. We then estimate the *y* value based on the mass change of graphite at different states of discharge and determine that one THF molecule is co-intercalated with one Li^+ (Fig. 2d). To provide additional support, we also added TGA experiments to quantify the number of THF in the ultimate co-intercalated structure[18]. After calculating the mass loss, we found that only one solvent was involved in t-THF-GIC after transformation (Fig. S17).

In summary, we have systematically demonstrated the *in-situ* b-GICs to t-GICs transformation under battery operating conditions, which is now schematically described in Fig. 2e. The THF electrolyte offers less aggressive co-intercalation chemistry compared to traditional glyme co-intercalation. The as-formed t-GICs with smaller interlayer spacing are highly reversible upon continuous electrochemical cycling, which informs the operation of Li^+-THF co-intercalation chemistry for extreme-condition batteries.

Electrolyte properties and solvation structure

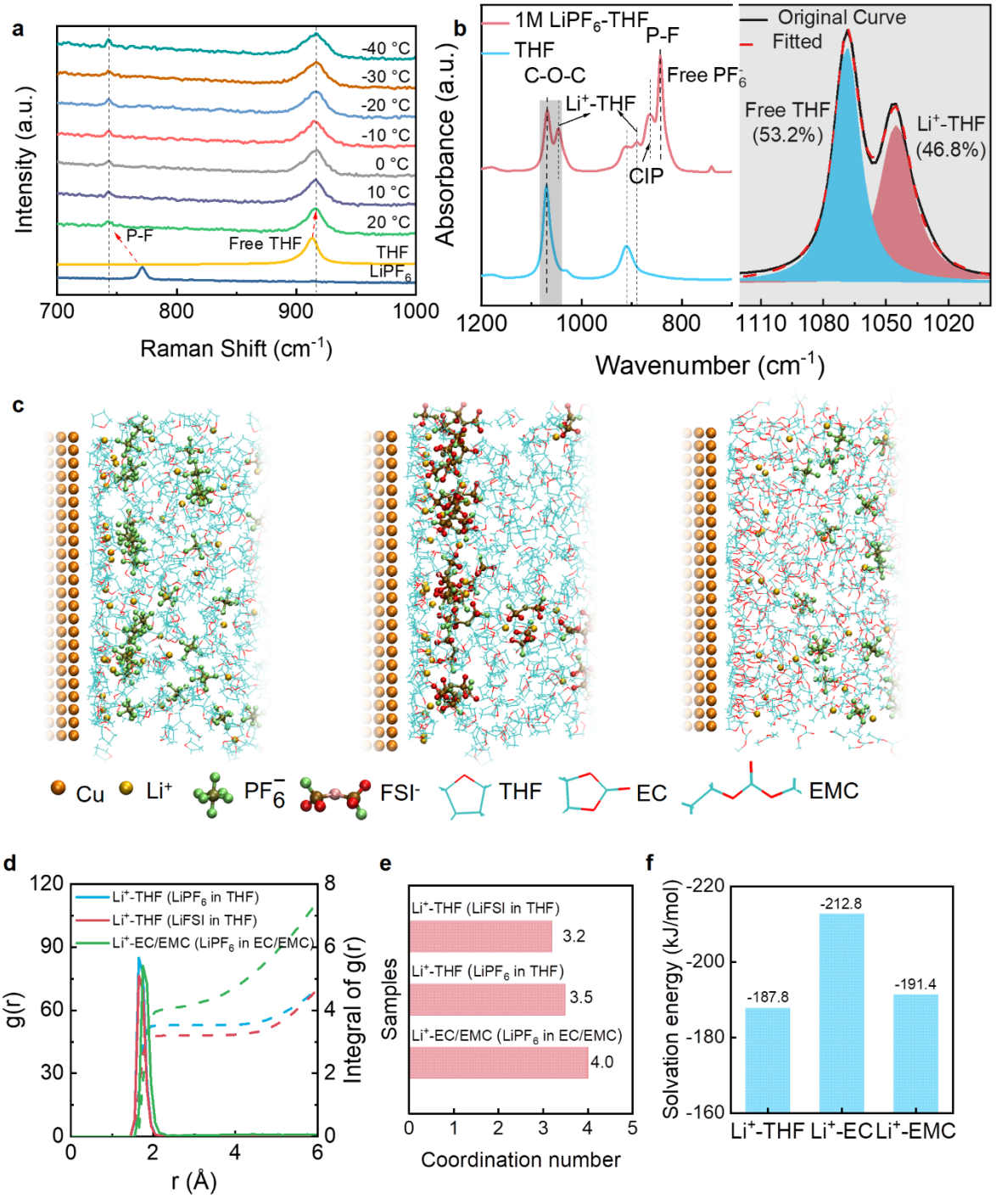

Fig. 3: Electrolyte properties and solvation structure. **a,** Raman spectroscopy of the 1M $LiPF_6$-THF at different temperatures. **b,** FTIR spectrum of the 1M $LiPF_6$-THF. **c,** The double-layer structure near the anode in 1 M $LiPF_6$-THF (left), 1 M LiFSI-THF (middle), and 1M $LiPF_6$-EC/EMC (right) electrolytes. The surface charge on the electrode is -0.1 C m^{-2}. **d,** The radial

distribution function g(r) and the integrated g(r) between the Li^+ in the double layer and the solvent molecules. **e,** The coordination number of the interfacial solvation structures. **f,** The solvation energy between Li^+ and different solvent molecules.

Next, we examine the physicochemical properties and solvation structure of the 1M $LiPF_6$-THF electrolyte. The electrolyte presents excellent ion conductivity in the range of 20 to -40 °C, much higher than that of the commercial carbonate electrolyte, especially in the low-temperature region (Fig. S18a). Moreover, the electrolyte remains clear with no salt precipitation and has good fluidity at -40 °C (Fig. S18b). Differential scanning calorimetry (DSC) further measures that the electrolyte maintains a liquid phase even at -103°C, highlighting sub-zero temperature applications (Fig. S18c). Besides the ion conductivity and viscosity, the solvation effect is also crucial for ion transport in batteries as it determines the desolvation kinetics and interphase properties[25–28]. Therefore, Raman spectroscopy and Fourier transform infrared spectroscopy (FTIR) are performed on the electrolyte. 1M LiFSI-THF and 1M $LiPF_6$-EC/EMC are used for comparison. **Fig. 3a** shows the Raman spectra of the 1M $LiPF_6$-THF electrolyte at different temperatures. Pure $LiPF_6$ salt displays one peak at 771 cm^{-1}, corresponding to the P-F stretching vibration. After dissolving in THF, the P-F peak shifts to 742 cm^{-1}, indicating the strong dissociation between Li^+ and PF_6^-. The THF ring breathing shifts from 913 cm^{-1} to 916 cm^{-1} after adding $LiPF_6$, indicating a weak interaction between THF and Li^+. More importantly, these shifted peaks remain at the same position after the temperature is decreased from 20 to -40 °C, suggesting the low-temperature stability of the electrolyte. For the LiFSI-THF electrolyte, the vibration band of THF still maintains at 913 cm^{-1}, indicating a weaker interaction between THF and Li^+ (Fig. S19a). Whereas the vibration band of the coordinated EC/EMC solvent is observed apparently, indicating a strong interaction between Li^+ and EC/EMC (Fig. S19b). Fig. 3b presents the FTIR result of the 1M $LiPF_6$-THF electrolyte. A clear contact ion pair (CIP) peak is observed at 864 cm^{-1}[29]. The C-O-C in THF is coordinated with Li^+ after introducing $LiPF_6$. Further fitting the peak ratio, the Li^+-THF content accounts for 46.8%.

Classical molecular dynamics (cMD) simulations are conducted to understand the dominating solvation structure at the anode surface in the electrolyte. Simulation boxes in cMD are constructed by sandwiching the electrolyte between two electrodes with a surface charge of ±0.1 C m^{-2}. The double-layer structure near the anode in these three electrolytes is shown in Fig. 3c. The

solvent|cation|anion layered structure is a result of the surface adsorption of the polar solvent molecules and the repelling Coulombic force to the anions. The Li^+-O radial distribution function *g(r)* analysis is performed by taking the first Li^+ layer adjacent to the anode as the central ion to study the interfacial solvation structures (Fig. 3d). According to the solvation number from the solvent molecules (Fig. 3e), THF-based electrolytes present the interfacial solvation structures dominated by a mixture of CIP and the solvent-separated ion pair (SSIP), while it is majorly SSIP in the EC/EMC-based electrolyte. As a result, the binding energy of Li^+-THF is smaller than that of Li^+-EC and Li^+-EMC (Fig. 3f). Thus, Li^+ can be readily desolvated from THF, decreasing the coordination number from Li^+-$(THF)_{3.5}$ to Li^+-$(THF)_1$ prior to co-intercalation.

Battery Performance

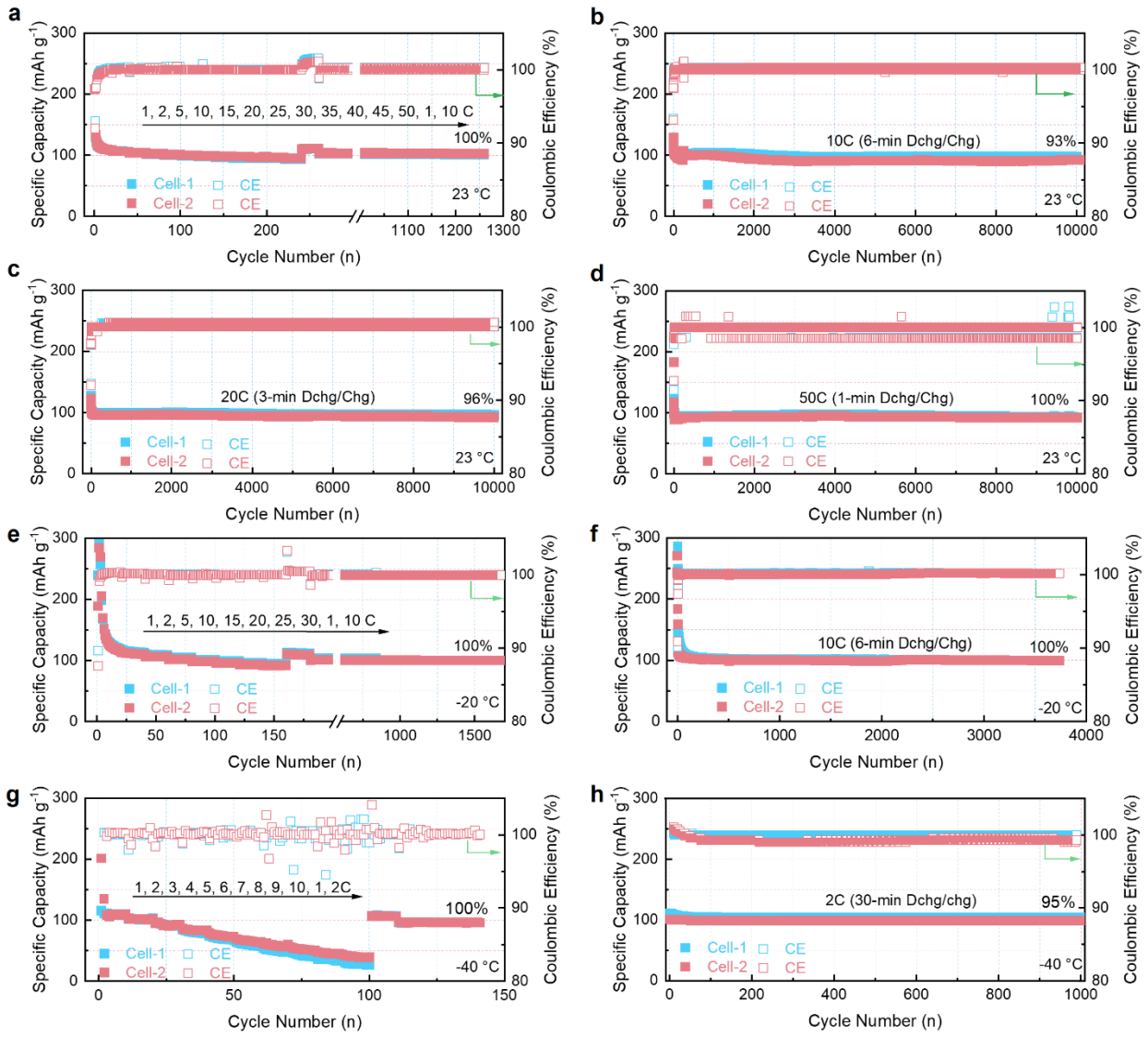

Fig. 4: G||Li cells under extreme conditions for extended cycling. a, Rate capability of G||Li cell at the current range of 1 to 50 C (1 C=100 mA g^{-1}), and then continue to cycle at 10 C after the rate performance. **b-d,** Long-term cycling performance of G||Li at 10 C, 20 C, and 50 C, respectively. **e,** Rate capability of G||Li cell at the current range of 1 to 30 C at -20 °C, and then continue to cycle at 10 C after the rate performance. **f,** Long-term cycling performance of G||Li cell at 10 C at -20 °C. **g,** Rate capability of G||Li cell at the current range of 1 to 10 C at -40 °C, and then continue to cycle at 2 C after the rate performance. **h,** Long-term cycling performance of G||Li cell at 2 C at -40 °C. Cell-1 and Cell-2 are repeated measurements under identical experimental conditions.

Our extensive kinetics analyses shown in Figure S20 demonstrate that $D_{Li^+\text{-THF}}$ of graphite is almost the same during cycling at 23 and -40 °C and that the Li^+-THF storage process in graphite is similar to surface-limited capacitive reaction allowing for fast charging. Then, the electrochemical performance of G||Li cell in the 1 M $LiPF_6$-THF electrolyte is tested at different current densities and temperatures. The rate capability of G||Li cell is shown in **Fig. 4a** and Fig. S21a, where the average reversible capacities are 110, 105, 100, 98, and 97 mAh g^{-1} at 1, 10, 20, 30, and 40 C, respectively. Even at 50 C, the reversible capacity reaches 93 mAh g^{-1}, ~85% of the capacity at 1 C, demonstrating the ultrafast kinetics of the Li^+-THF co-intercalation. After returning to 1 C, the reversible capacity maintains its original value and can be further cycled 1,000 times at 10 C without capacity fading (**Fig. 4a**). The new G||Li cell can be cycled 10,000 times at 10 C with a capacity retention of 93%, indicating the superior stability of the Li^+-THF co-intercalation (Fig. 4b, Fig. S21b). Fig. 4c-d exhibits the ultralong cycling stability of the G||Li cell under ultrafast charging. At 20 C (3 mins discharge/charge), the G||Li cell delivers a reversible capacity of 100 mAh g^{-1} and is cycled stably 10,000 times with 96% capacity retention (Fig. 4c, Fig. S21c). Further increasing to 50 C (1 min discharge/charge), the G||Li cell still can maintain a high reversible capacity of 92 mAh g^{-1} after 10,000 cycles, with no capacity decay compared to the initial capacity (Fig. 4d, Fig. S21d). The low-temperature fast charging is further demonstrated in Fig. 4e-h. When cycled at -20 °C, the G||Li cell delivers reversible capacities of 111, 101, 95, and 91 mAh g^{-1} at 1, 10, 20, and 30 C, respectively, barely different from the room-temperature capacity (Fig. 4e, Fig. S21e). When cycled at 10 C, the G||Li cell maintains superior cycling stability with a reversible capacity of 100 mAh g^{-1} for 3,700 cycles at -20 °C, consistent with the initial capacity (Fig. 4f, Fig. S21f). Further cooling down to -40 °C, the reversible capacity at 1, 2, 5, and 10 C are 110, 102, 75, and 40 mAh g^{-1}, respectively (Fig. 4g, Fig. S21g). Although the rate capability decreases, the reversible capacities at 1 and 2 C are almost the same as room temperature, highlighting the excellent low-temperature fast charging performance (Fig. 4g). Moreover, the G||Li cell shows excellent cycling stability for 1,000 cycles at 2 C with 100% capacity retention (Fig. 4h, Fig. S21h). The electrochemical performance of the G||Li cell is further summarized in Fig. S21i. Such ultrafast charging performance at room and low temperatures has never been reported in graphite anodes elsewhere (Fig. S21j and Table S1). The morphological evolution of the cycled graphite is characterized by SEM images. After 100 cycles, the severe expansion of the graphite layer can be clearly observed in Figure S21, but the overall structure is still well preserved

without obvious exfoliation, showing its high mechanical stability. Moreover, there is no Li plating and "dead Li" formation on the graphite surface or in the separator (Fig. S22a-c). The EDS mapping shows that C, F, P, and O elements are well distributed on the surface of the cycled graphite, and the C content accounts for 91.7%, indicating that the electrolyte is stable without excessive decomposition (Fig. S22e).

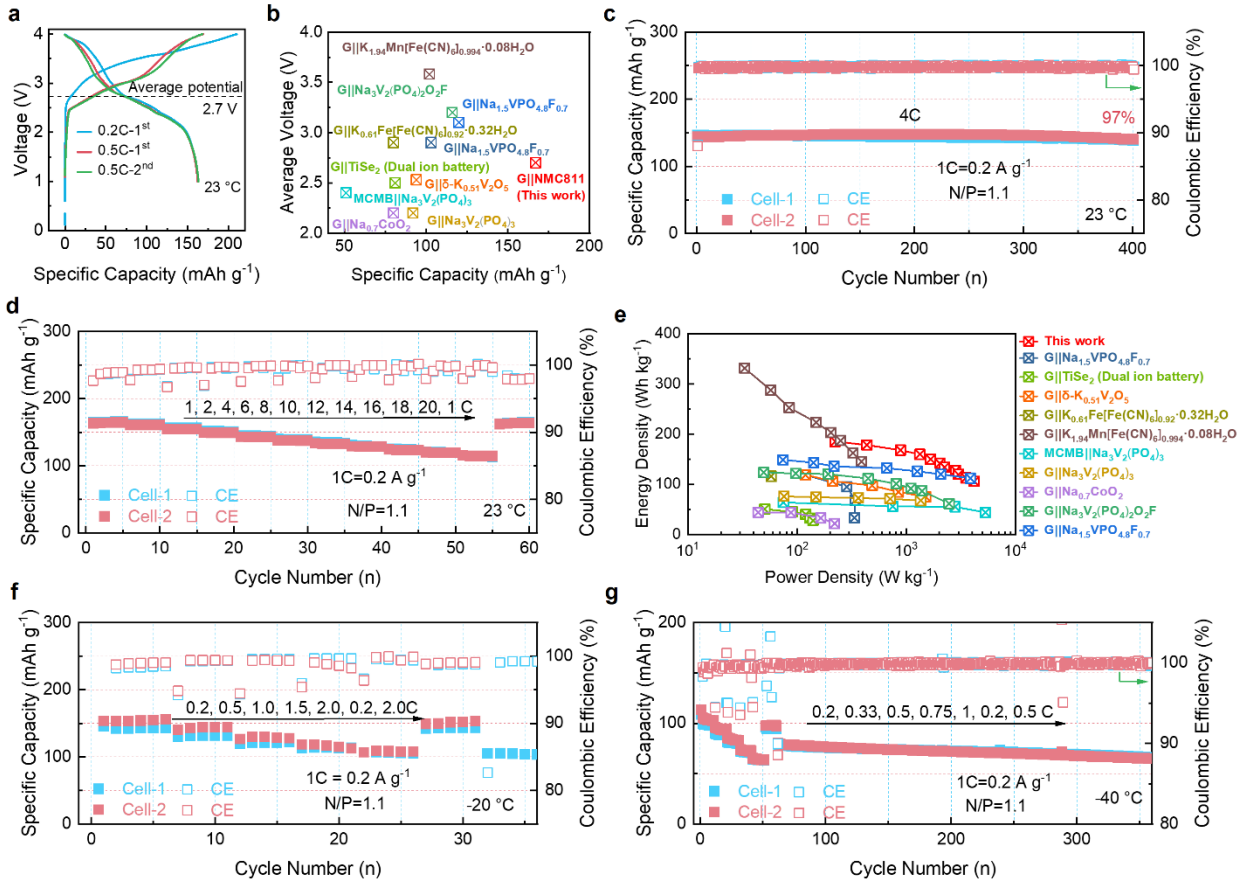

Fig. 5: High power density and high energy density Li-ion full cells. a, Voltage profiles of the G||NMC811 full cell at 0.2 C and 0.5 C (1C=0.2 A g^{-1}). **b,** Comparison of average voltage and capacity of the G||NMC811 full cell (based on the cathode) with recently reported Na-/K-based full cells[6,21,30–37]. **c**, Long-term cycling performance of the G||NMC811 full cell at 4 C. Full cell operation at 23 °C. **d,** Rate capability of the G||NMC811 full cell at the current range of 1 to 20 C. Full cell operation at 23 °C. **e,** Comparison of energy density and power density of the G||NMC811 full cell (based on the total mass of cathode and anode) with recently reported Na-/K-based full cell [6,21,30–37]. **f,** Rate capability of the G||NMC811 cell at the current range of 0.2 to 2 C. Full cell operation at -20 °C. g, Rate capability of the G||NMC811 cell at the current range of 0.2 to 1 C,

and then continue to cycle at 0.5 C after the rate performance. Full cell operation at -40 °C. Cell-1 and Cell-2 are repeated measurements under identical experimental conditions.

To evaluate the fast-charging and low-temperature performance of graphite anode in Li-ion full cells, NMC811 is selected as the cathode for full cells. No pre-cycled process is required since the graphite anode has high ICEs in the 1M $LiPF_6$-THF electrolyte, which is superior to the recently reported co-intercalation cells (Table S2). Three formation cycles are performed with one cycle at 0.2 C, then two cycles at 0.5 C (1C = 0.2 A g^{-1}) (Fig. 5a). The full cell delivers a capacity of 163 mA g^{-1} based on the mass of the cathode, with an average voltage of ~2.7 V at 0.5 C. The capacity is much higher than Na-based or K-based cells (Fig. 5b). As shown in Fig. S23, the full cell delivers an initial capacity of 133 mAh g^{-1} at 4 C when only a constant current charging (CCC) is performed. After 800 cycles, the full cell remains a reversible capacity of 123 mAh g^{-1}, with an extremely low capacity decay rate of 0.009% per cycle, validating the high stability of NMC811 and graphite in the 1M $LiPF_6$-THF electrolyte. When a constant voltage charging (CVC) procedure is added to the CCC step for a complete charging process of 15 minutes. The full cell delivers a high initial capacity of 146 mAh g^{-1} at 4 C with a capacity retention of 97% after 400 cycles (Fig. 5c). Fig. 5d displays the rate capability of the full cell at current densities ranging from 1 to 20 C (1.5 mins charging process), where the reversible capacities are 167, 163, 157, 151, 145, 139, 134, 129, 125, 120, and 114 mAh g^{-1}, respectively (Fig. S24a). Approximately 68% of the reversible capacity is retained even with a 20-fold increase in current density from 1 to 20 C. The high rate capability renders a remarkably high-power density of 4,180 W kg^{-1} with an energy density of 106 Wh kg^{-1} (Fig. 5e, based on the total mass of the cathode and anode), much higher than Na-based and K-based cells (Table S2). The low temperature (and fast charging) performance is further tested. The full cell also shows excellent rate performance at -20 °C, delivering 142, 131, 120, 113, and 105 mAh g^{-1} at 0.2, 0.5, 1.0, 1.5, and 2.0 C, respectively (Fig. 5f, Fig. S24b). An impressive capacity (134 mA g^{-1}) and stability (~92%) are also obtained after 150 cycles at 1 C (Fig. S25a, S25b). Even at -40 °C, the full cell using 1M $LiPF_6$-THF electrolyte exhibits excellent rate performance (Fig. 5g, Fig. S24c). As shown in Fig. 5g, the reversible capacities are determined to be 101, 91, 80, 69, and 61 mAh g^{-1} at 0.2, 0.333, 0.5, 0.75, and 1 C, respectively. Continuing cycling at 0.2 C, the full cell maintains 83% of its initial capacity after 150 cycles (Fig. S25c-d). Switching cycling to 0.5 C, the full cell retains 84% capacity retention after 300 cycles (Fig. 5g, Fig. S24c). Such excellent low-temperature performance has never been reported in Li-ion full cells to date (Table S3).

Conclusion

In this work, we discover a new intercalation chemistry superior to traditional glyme co-intercalation. t-GICs are *in situ* synthesized in the 1M $LiPF_6$-THF electrolyte via a controllable chemical reaction between b-GIC and THF during battery cycling, which enables reversible, rapid Li^+-THF co-intercalation into graphite. The *operando* X-ray and electrochemical analyses further confirmed this spontaneous synthesis. Compared to linear ether, cyclic ether has a weak interaction with Li^+ due to the steric hindrance, which allows for facile partial desolvation of Li^+-$(THF)_{3.5}$ to yield Li^+-$(THF)_1$ for rapid co-intercalation. Our electrolyte has also made battery reactions in individual graphite particles proceed synchronously even at fast charging. As a result, the graphite anode displays an ultralong lifespan of over 10,000 cycles with negligible capacity decay, 1-minute fast charging, and unprecedented low-temperature performance (including fast charging) with no lithium dendrite formation. Coupled with the NMC cathode, the full cell displays an excellent balance between energy and power in the Ragone plot and outstanding cycling stability for 800 cycles within 15 mins charging. Even at -40 °C, the excellent rate capability can be achieved, with 100 mAh g^{-1} at 0.1 C, 90 mAh g^{-1} at 0.33 C, 80 mAh g^{-1} at 0.5 C, and 60 mAh g^{-1} at 1 C, respectively. Graphite anode with such high-power capability in LIBs has never been reported elsewhere. THF is a low-cost, mass-produced chemical, making 1M $LiPF_6$-THF an attractive electrolyte for commercialization. Last but not least, our work provides new insights into GICs synthesis and opens the door to designing beyond-graphite intercalation anodes for fast charging and low-temperature operations.

Data Availability Statement

All relevant data in the article are available from the corresponding author upon reasonable request.

Supporting Information

The Supporting Information is available free of charge at acs.org.

Materials and Methods, electrochemical measurements, *Operando* synchrotron XRD, *Operando* CMCD, Raman, SEM, and TEM images.

Author Contributions

L.T. and D.X. contributed equally to the work.

Notes

The authors declare no competing financial interest.

Acknowledgments

The work was supported by the USDA AFRI Foundational and Applied Program (grant number 2020-67021-31139), the Sun Grant program of the National Institute of Food and Agriculture (NIFA), USDA, USA, and the Institute for Critical Technology and Applied Science at Virginia Tech. The material characterization experiments were partly supported by IMSE (Institute of Materials Science and Engineering) at Washington University in Saint Louis (WUSTL). P.B. acknowledges the faculty startup support from WUSTL, a gift fund from TSVC, and the National Science Foundation grant (Award No. 1934122). P.S. acknowledges the fellowship support from the McDonnell International Scholars Academy at WUSTL. F.S. acknowledges the National Science Foundation grant (Award No. 2239690). This research used electron microscopy resources of the Center for Functional Nanomaterials (CFN), which is a U.S. Department of Energy Office of Science User Facility, at Brookhaven National Laboratory under Contract No. DE-SC0012704. FTIR performed at ORNL was financially supported by Dr. Imre Gyuk from the Energy Storage Program, Office of Electricity, Department of Energy. We appreciate CAMP (Cell Analysis, Modeling, and Prototyping) for supplying graphite powder and electrodes. We also appreciate Qian Wang for the TGA measurement.

References

(1) Li, Y.; Lu, Y.; Adelhelm, P.; Titirici, M. M.; Hu, Y. S. Intercalation Chemistry of Graphite: Alkali Metal Ions and Beyond. *Chem. Soc. Rev.* **2019**, *48* (17), 4655–4687.

(2) Dresselhaus, M. S.; Dresselhaus, G. Intercalation Compounds of Graphite. *Adv. Phys.* **2002**, *51* (1), 1–186.

(3) Enoki, T.; Suzuki, M.; Endo, M. Graphite Intercalation Compounds and Applications. Oxford University Press, **2003**.

(4) Xu, J.; Dou, Y.; Wei, Z.; Ma, J.; Deng, Y.; Li, Y.; Liu, H.; Dou, S. Recent Progress in Graphite Intercalation Compounds for Rechargeable Metal (Li, Na, K, Al)-Ion Batteries. *Adv. Sci.* **2017**, *4* (10), 1700146.

(5) Seel, J. A.; Dahn, J. R. Electrochemical Intercalation of PF_6 into Graphite. *J. Electrochem. Soc.* **2000**, *147* (3), 892.

(6) Xu, Z. L.; Yoon, G.; Park, K. Y.; Park, H.; Tamwattana, O.; Joo Kim, S.; Seong, W. M.; Kang, K. Tailoring Sodium Intercalation in Graphite for High Energy and Power Sodium Ion Batteries. *Nat. Commun.* **2019**, *10* (1), 2598.

(7) Nishi, Y. Lithium Ion Secondary Batteries; Past 10 Years and the Future. *J. Power Sources* **2001**, *100* (1–2), 101–106.

(8) Lagrange, P. Overview on the Chemistry of Intercalation into Graphite of Binary Metallic Alloys. *Chemical Physics of Intercalation II Springer*, **1993**, 303–310.

(9) Basu, S.; Zeller, C.; Flanders, P. J.; Fuerst, C. D.; Johnson, W. D.; Fischer, J. E. Synthesis and Properties of Lithium-Graphite Intercalation Compounds. *Mater. Sci. Eng.* **1979**, *38* (3), 275–283.

(10) Shu, Z. X.; McMillan, R. S.; Murray, J. J. Electrochemical Intercalation of Lithium into Graphite. *J. Electrochem. Soc.* **1993**, *140* (4), 922–927.

(11) Fong, R.; von Sacken, U.; Dahn, J. R. Studies of Lithium Intercalation into Carbons Using Nonaqueous Electrochemical Cells. *J. Electrochem. Soc.* **1990**, *137* (7), 2009–2013.

(12) Xu, K. Li-Ion Battery Electrolytes. *Nat. Energy* **2021**, *6* (7), 763–763.

(13) An, S. J.; Li, J.; Daniel, C.; Mohanty, D.; Nagpure, S.; Wood, D. L. The State of Understanding of the Lithium-Ion-Battery Graphite Solid Electrolyte Interphase (SEI) and Its Relationship to Formation Cycling. *Carbon* **2016**, *105*, 52–76.

(14) Jache, B.; Adelhelm, P. Use of Graphite as a Highly Reversible Electrode with Superior Cycle Life for Sodium-Ion Batteries by Making Use of Co-Intercalation Phenomena. *Angew. Chem. Int. Ed.* **2014**, *53* (38), 10169–10173.

(15) Kim, H.; Lim, K.; Yoon, G.; Park, J. H.; Ku, K.; Lim, H. D.; Sung, Y. E.; Kang, K. Exploiting Lithium–Ether Co-Intercalation in Graphite for High-Power Lithium-Ion Batteries. *Adv. Energy Mater.* **2017**, *7* (19), 1700418.

(16) Choi, J.; Jeong, H.; Jang, J.; Jeon, A. R.; Kang, I.; Kwon, M.; Hong, J.; Lee, M. Weakly Solvating Solution Enables Chemical Prelithiation of Graphite-SiOx Anodes for High-Energy Li-Ion Batteries. *J. Am. Chem. Soc.* **2021**, *143* (24), 9169–9176.

(17) Xia, D.; Kamphaus, E. P.; Hu, A.; Hwang, S.; Tao, L.; Sainio, S.; Nordlund, D.; Fu, Y.; Huang, H.; Cheng, L.; Lin, F. Design Criteria of Dilute Ether Electrolytes toward Reversible and Fast Intercalation Chemistry of Graphite Anode in Li-Ion Batteries. *ACS Energy Lett.* **2023**, *8* (3), 1379–1389.

(18) Beguin, F.; Setton, R.; Beguin, F.; Setton, R.; Hamwi, A.; Touzain, P. The Reversible Intercalation of Tetrahydrofuran in Some Graphite-Alkali Metal Lamellar Compounds. *Mater. Sci. Eng.* **1979**, *40* (2), 167–173.

(19) Yang, Y.; Chen, Y.; Tan, L.; Zhang, J.; Li, N.; Ji, X.; Zhu, Y. Rechargeable $LiNi_{0.65}Co_{0.15}Mn_{0.2}O_2$||Graphite Batteries Operating at −60 °C. *Angew. Chem. Int. Ed.* **2022**, *61* (42), e202209619.

(20) Li, L.; Liu, L.; Hu, Z.; Lu, Y.; Liu, Q.; Jin, S.; Zhang, Q.; Zhao, S.; Chou, S. L. Understanding High-Rate K+-Solvent Co-Intercalation in Natural Graphite for Potassium-Ion Batteries. *Angew. Chem. Int. Ed.* **2020**, *59* (31), 12917–12924.

(21) Kim, H.; Hong, J.; Park, Y. U.; Kim, J.; Hwang, I.; Kang, K. Sodium Storage Behavior in Natural Graphite Using Ether-Based Electrolyte Systems. *Adv. Funct. Mater.* **2015**, *25* (4), 534–541.

(22) Yoon, G.; Kim, H.; Park, I.; Kang, K.; Yoon, G.; Kim, H.; Park, I.; Kang, K. Conditions for Reversible Na Intercalation in Graphite: Theoretical Studies on the Interplay Among Guest Ions, Solvent, and Graphite Host. *Adv. Energy Mater.* **2017**, *7* (2), 1601519.

(23) Yamada, Y.; Usui, K.; Chiang, C. H.; Kikuchi, K.; Furukawa, K.; Yamada, A. General Observation of Lithium Intercalation into Graphite in Ethylene-Carbonate-Free Superconcentrated Electrolytes. *ACS Appl. Mater. Interfaces* **2014**. *6(14)*, 10892-10899.

(24) Xia, D.; Jeong, H.; Hou, D.; Tao, L.; Li, T.; Knight, K.; Hu, A.; Kamphaus, E. P.; Nordlund, D.; Sainio, S.; Liu, Y.; Morris, J. R.; Xu, W.; Huang, H.; Li, L.; Xiong, H.; Cheng, L.; Lin, F. Self-Terminating, Heterogeneous Solid–Electrolyte Interphase Enables Reversible Li–Ether Cointercalation in Graphite Anodes. *Proc. Natl. Acad. Sci.* **2024**, *121* (5), e2313096121.

(25) Xu, K. Electrolytes and Interphases in Li-Ion Batteries and Beyond. *Chem. Rev.* **2014**, *114* (23), 11503–11618.

(26) Wang, H.; Kim, S. C.; Tomás, Ş; Rojas, T.; Zhu, Y.; Li, Y.; Ma, L.; Xu, K.; Ngo, A. T.; Cui, Y. Correlating Li-Ion Solvation Structures and Electrode Potential Temperature Coefficients. *J. Am. Chem. Soc* **2021**, *143(5)*, 2264-2271.

(27) Li, M.; Wang, C.; Chen, Z.; Xu, K.; Lu, J. New Concepts in Electrolytes. *Chem. Rev*. **2020**, *120(14),* 6783-6819.

(28) Xu, J.; Zhang, J.; Pollard, T. P.; Li, Q.; Tan, S.; Hou, S.; Wan, H.; Chen, F.; He, H.; Hu, E.; Xu, K.; Yang, X. Q.; Borodin, O.; Wang, C. Electrolyte Design for Li-Ion Batteries under Extreme Operating Conditions. *Nature* **2023**, *614* (7949), 694–700.

(29) Zou, Y.; Ma, Z.; Liu, G.; Li, Q.; Yin, D.; Shi, X.; Cao, Z.; Tian, Z.; Kim, H.; Guo, Y.; Sun, C.; Cavallo, L.; Wang, L.; Alshareef, H. N.; Sun, Y.-K.; Ming, J. Non-Flammable Electrolyte Enables High-Voltage and Wide-Temperature Lithium-Ion Batteries with Fast Charging. *Angew. Chem. Int. Ed.* **2023**, *135* (8), e202216189.

(30) Liang, H. J.; Gu, Z. Y.; Zhao, X. X.; Guo, J. Z.; Yang, J. L.; Li, W. H.; Li, B.; Liu, Z. M.; Li, W. L.; Wu, X. L. Ether-Based Electrolyte Chemistry Towards High-Voltage and Long-Life Na-Ion Full Batteries. *Angew. Chem. Int. Ed.* **2021**, *60* (51), 26837–26846.

(31) Hasa, I.; Dou, X.; Buchholz, D.; Shao-Horn, Y.; Hassoun, J.; Passerini, S.; Scrosati, B. A Sodium-Ion Battery Exploiting Layered Oxide Cathode, Graphite Anode and Glyme-Based Electrolyte. *J. Power Sources* **2016**, *310*, 26–31.

(32) Zhu, Z.; Cheng, F.; Hu, Z.; Niu, Z.; Chen, J. Highly Stable and Ultrafast Electrode Reaction of Graphite for Sodium Ion Batteries. *J. Power Sources* **2015**, *293*, 626–634.

(33) Wei, Q.; Chang, X.; Wang, J.; Huang, T.; Huang, X.; Yu, J.; Zheng, H.; Chen, J.-H.; Peng, D.-L.; Wei, Q.; Chang, X.; Wang, J.; Huang, T.; Huang, X.; Yu, J.; Zheng, H.; Peng, D.-L.; Chen, J.-H. An Ultrahigh-Power Mesocarbon Microbeads|Na^+-Diglyme|$Na_3V_2(PO_4)_3$ Sodium-Ion Battery. *Adv. Mater.* **2022**, *34* (6), 2108304.

(34) Deng, L.; Qu, J.; Niu, X.; Liu, J.; Zhang, J.; Hong, Y.; Feng, M.; Wang, J.; Hu, M.; Zeng, L.; Zhang, Q.; Guo, L.; Zhu, Y. Defect-Free Potassium Manganese Hexacyanoferrate Cathode Material for High-Performance Potassium-Ion Batteries. *Nat. Commun.* **2021**, *12* (1), 2167.

(35) Zhu, Y. H.; Yang, X.; Bao, D.; Bie, X. F.; Sun, T.; Wang, S.; Jiang, Y. S.; Zhang, X. B.; Yan, J. M.; Jiang, Q. High-Energy-Density Flexible Potassium-Ion Battery Based on Patterned Electrodes. *Joule* **2018**, *2* (4), 736–746.

(36) Zhu, Y. H.; Zhang, Q.; Yang, X.; Zhao, E. Y.; Sun, T.; Zhang, X. B.; Wang, S.; Yu, X. Q.; Yan, J. M.; Jiang, Q. Reconstructed Orthorhombic V_2O_5 Polyhedra for Fast Ion Diffusion in K-Ion Batteries. *Chem* **2019**, *5* (1), 168–179.

(37) Zheng, R.; Yu, H.; Zhang, X.; Ding, Y.; Xia, M.; Cao, K.; Shu, J.; Vlad, A.; Su, B. L. A $TiSe_2$-Graphite Dual Ion Battery: Fast Na-Ion Insertion and Excellent Stability. *Angew. Chem. Int. Ed.* **2021**, *60* (34), 18430–18437.

TOC

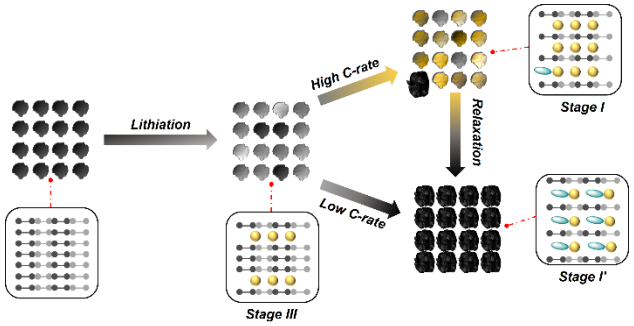
Lithiation
High C-rate
Relaxation
Low C-rate
Stage I
Stage I'
Stage III